Isovector axial form factor of the nucleon from lattice QCD

Dalibor Djukanovic,[1,2] Georg von Hippel,[3] Jonna Koponen,[3] Harvey B. Meyer,[1,3] Konstantin Ottnad,[3] Tobias Schulz,[3] and Hartmut Wittig[1,3]

[1]*Helmholtz-Institut Mainz, Johannes Gutenberg-Universität Mainz, D-55099 Mainz, Germany*
[2]*GSI Helmholtzzentrum für Schwerionenforschung, Darmstadt 64291, Germany*
[3]*PRISMA$^+$ Cluster of Excellence & Institut für Kernphysik, Johannes Gutenberg-Universität Mainz, D-55099 Mainz, Germany*

(Received 12 July 2022; accepted 28 September 2022; published 14 October 2022)

The isovector axial form factor of the nucleon plays a key role in interpreting data from long-baseline neutrino oscillation experiments. We perform a lattice-QCD based calculation of this form factor, introducing a new method to directly extract its z expansion from lattice correlators. Our final parametrization of the form factor, which extends up to spacelike virtualities of 0.7 GeV^2 with fully quantified uncertainties, agrees with previous lattice calculations but is significantly less steep than neutrino-deuterium scattering data suggests.

DOI: 10.1103/PhysRevD.106.074503

I. INTRODUCTION

The axial form factor of the nucleon $G_{\mathrm{A}}(Q^2)$ plays a central role in understanding the quasielastic part of GeV-scale neutrino-nucleus cross sections. Particularly for the upcoming long-baseline neutrino oscillation experiments DUNE [1] and T2HK [2], these cross sections must be known with few-percent uncertainties [3] to enable a sufficiently reliable reconstruction of the incident neutrino energy. In the absence of modern, high-quality experimental measurements of $G_{\mathrm{A}}(Q^2)$ [4], calculations for the axial form factor from lattice QCD [5] are of crucial importance in order to maximize the scientific output of neutrino-oscillation experiments.

For a long time, the axial charge of the nucleon, $g_A \equiv G_{\mathrm{A}}(0)$, has served as a benchmark quantity for lattice QCD calculations [6], exemplifying the improvements of recent years in terms of control over statistical and systematic errors. The latter are caused mainly by the excited-state contamination in Euclidean correlation functions [7–10], as well as by the chiral and continuum extrapolation. Many of the techniques developed have been carried over and applied to nonvanishing momentum transfer Q^2, most recently in Refs. [11–16]. In comparison to the calculation of the charge, a new source of systematics arises for the form factor, namely the parametrization of the Q^2 dependence. Historically, an *ad hoc* dipole *Ansatz* was used (see Ref. [4]), incurring an unquantified model systematic. As a modern alternative, an *Ansatz* based on the z expansion has been used extensively, leading to less model bias at the cost of an increased statistical error on the phenomenological determination of the mean square radius $\langle r_{\mathrm{A}}^2 \rangle = [\frac{-6}{G_{\mathrm{A}}} \frac{dG_{\mathrm{A}}}{dQ^2}]_{Q^2=0}$ [17]. The sensitivity to the parametrization is also visible in lattice calculations, where the different *Ansätze* lead to inconsistent results (see e.g., [13]).

In this article, we perform a high-statistics calculation of $G_{\mathrm{A}}(Q^2)$ for momentum transfers up to 0.7 GeV^2 using lattice simulations with dynamical up, down and strange quarks with an $\mathrm{O}(a)$ improved Wilson fermion action. We employ a new analysis method that simultaneously handles the issues of the excited-state contamination and the description of the form factor's Q^2 dependence.

II. METHODOLOGY

The matrix elements of the local isovector axial current $A_\mu^a(x) = \bar{\psi}\gamma_\mu\gamma_5\frac{\tau^a}{2}\psi$ between single-nucleon states are parametrized by the axial form factor $G_{\mathrm{A}}(Q^2)$ and induced pseudoscalar form factor $G_{\mathrm{P}}(Q^2)$. We focus on the current component orthogonal to the momentum transfer, thereby projecting onto the axial form factor,

$$\langle N(p',s')|\vec{q}\times\vec{A}^a(0)|N(p,s)\rangle = G_{\mathrm{A}}(Q^2)\bar{U}^{s'}(p')\vec{q}\times\vec{\gamma}\gamma_5\frac{\tau^a}{2}U^s(p), \quad (1)$$

where $\vec{q} = \vec{p}' - \vec{p}$, $Q^2 = \vec{q}^2 - (E_{p'} - E_p)^2$ and $U^s(p)$ is an isodoublet Dirac spinor with momentum p and spin state s. We employ Euclidean notation throughout.

The setup for our lattice determination of the axial form factor is very similar to the one we used in the case of the electromagnetic form factors [18]. The nucleon two- and three-point functions are computed as

$$C_2(\vec{p},t) = a^3 \sum_{\vec{x}} e^{i\vec{p}\cdot\vec{x}} \Gamma_{\beta\alpha} \langle \Psi^\alpha(t,\vec{x}) \bar{\Psi}^\beta(0) \rangle, \tag{2}$$

$$C_3(\vec{q},t,t_s) = -ia^6 \sum_{\vec{x},\vec{y}} e^{i\vec{q}\cdot\vec{y}} \Gamma_{\beta\alpha} \frac{\vec{q}\times\vec{s}}{|\vec{q}\times\vec{s}|^2} \cdot \langle \Psi^\alpha(t_s,\vec{x}) \vec{q}\times\vec{A}^{a=3}(t,\vec{y}) \bar{\Psi}^\beta(0) \rangle, \tag{3}$$

where $\Psi^\alpha(\vec{x},t)$ denotes the proton interpolating operator

$$\Psi^\alpha(x) = \epsilon_{abc} (\tilde{u}_a^T(x) C\gamma_5 \tilde{d}_b(x)) \tilde{u}_c^\alpha(x). \tag{4}$$

The quark fields $\tilde{u}$, $\tilde{d}$ are smeared with a Gaussian kernel [19], using APE-smeared gauge fields [20], in such a way that the smearing radius remains approximately constant as a function of the lattice spacing. The nucleon mass is extracted via a one-exponential fit to $C_2(\vec{0},t)$, and the relativistic dispersion relation is used for E_p. We have chosen to compute the nucleon three-point function in the rest frame of the final-state nucleon, $\vec{p}' = 0$, and the chosen projection matrix Γ reads[1]

$$\Gamma = \frac{1}{2}(1+\gamma_0)(1+i\gamma_5 \vec{s}\cdot\vec{\gamma}). \tag{5}$$

In practice, we have set $\vec{s} = \vec{e}_3$, i.e., the nucleon spin is aligned along the x_3 axis. The transverse part $\vec{q}\times\vec{A}^a$ of the axial current receives no additive $\mathrm{O}(a)$ improvement. For its multiplicative renormalization, we employ the determination of Z_A and b_A from [21,22], respectively, while the coefficient $\tilde{b}_A$ in the notation of [22] is neglected, since it parametrizes a sea-quark effect and is expected to be small.

The accessible momentum transfers are discrete, $\vec{q} = 2\pi\vec{n}/L$, $\vec{n} \in \mathbb{Z}^3$ in a periodic box of size $L \times L \times L$. For a given value of $\mathfrak{q} = 2\pi|\vec{n}|/L$, we perform averages of the two-point functions over all spatial momenta $\vec{q}$ of norm $\mathfrak{q}$,

$$\bar{C}_2(\mathfrak{q},t) = \sum_{\vec{q}:|\vec{q}|=\mathfrak{q}} C_2(\vec{q},t) \Big/ \Big(\sum_{\vec{q}:|\vec{q}|=\mathfrak{q}} 1 \Big). \tag{6}$$

We then use the ratio

$$R(\vec{q},t,t_s) \equiv \frac{C_3(\vec{q},t,t_s)}{\bar{C}_2(0,t_s)} \sqrt{\frac{\bar{C}_2(|\vec{q}|,t_s-t)\bar{C}_2(0,t)\bar{C}_2(0,t_s)}{\bar{C}_2(0,t_s-t)\bar{C}_2(|\vec{q}|,t)\bar{C}_2(|\vec{q}|,t_s)}} \tag{7}$$

to build a momentum-averaged estimator for $G_\mathrm{A}(Q^2)$,

$$G_\mathrm{A}^\mathrm{eff}(\mathfrak{q};t,t_s) = \sqrt{\frac{2E_\mathfrak{q}}{m+E_\mathfrak{q}}} \sum_{\vec{q}:|\vec{q}|=\mathfrak{q}}{}' R(\vec{q},t,t_s) \Big/ \Big(\sum_{\vec{q}:|\vec{q}|=\mathfrak{q}}{}' 1 \Big), \tag{8}$$

where the prime on the sum indicates that we impose the additional constraint $|q_3| \le \min(|q_1|,|q_2|)$, which we have found to slightly improve the signal. From here we construct the summed insertion

$$S(\mathfrak{q},t_s) \equiv a \sum_{t=a}^{t_s-a} G_\mathrm{A}^\mathrm{eff}(\mathfrak{q};t,t_s), \overset{t_s\to\infty}{=} b_0(\mathfrak{q}) + t_s G_\mathrm{A}(Q^2) + \ldots, \tag{9}$$

with $Q^2 = \mathfrak{q}^2 - (m - E_\mathfrak{q})^2$. The dots stand for excited-state contributions that are of order $e^{-\Delta t_s}$ and $t_s e^{-\Delta t_s}$, with Δ the energy gap above the single-nucleon state.

As a novelty, we introduce a technique which is based on fitting simultaneously the $\mathfrak{q}$ and t_s dependence of $S(\mathfrak{q},t_s)$, by parametrizing the axial form factor from the outset via the z expansion (see [17,23] and Refs. therein),

$$G_\mathrm{A}(Q^2) = \sum_{n=0}^{n_\mathrm{max}} a_n z^n(Q^2), \tag{10}$$

$$z(Q^2) = \frac{\sqrt{t_\mathrm{cut}+Q^2} - \sqrt{t_\mathrm{cut}}}{\sqrt{t_\mathrm{cut}+Q^2} + \sqrt{t_\mathrm{cut}}}. \tag{11}$$

The fit parameters are the coefficients a_n and the offsets $b_0(\mathfrak{q})$, which we keep as independent fit parameters for each value of $\mathfrak{q}$. In the data analyzed below, we set $n_\mathrm{max} = 2$ without constraining the fit parameters by priors. We note that setting $n_\mathrm{max} = 3$ would require the use of priors for the highest-order term to stabilize the fit, but the results are consistent with our preferred $n_\mathrm{max} = 2$ results. To obtain the form factor at the physical point, the a_n are extrapolated to the continuum and interpolated to the physical pion mass, at which point the form factor may be evaluated at any virtuality in the chosen expansion interval $[0, 0.7\ \mathrm{GeV}^2]$.

Our method relies on the fact that, for a given Q^2 interval, the z expansion represents a general, systematically improvable parametrization of the form factor [23]. We have chosen to map $Q^2 = 0$ to the point $z = 0$ and set $t_\mathrm{cut} = (3M_\pi^\mathrm{phys})^2$ to the three-pion kinematic threshold at the physical pion mass for all gauge ensembles used, as this choice reduces the pion-mass dependence of the a_n. We find that the immediate parametrization of the form factor

[1]We have used the projection matrix given in Eq. (5) throughout the calculation, with the exception of the nucleon mass determination, for which we used the unpolarized projection matrix $\Gamma = (1+\gamma_0)/2$.

has a stabilizing effect as compared to the standard two-step procedure of first obtaining the form factor independently at discrete values of Q^2, followed by a continuous parametrization of these data points. We return to this point in the next section.

We perform fits to $S(\mathbf{q}, t_s)$ based on the second line of Eq. (9), dropping the omitted terms, and including all values of t_s greater than or equal to a certain $t_s^{\min}$. We perform these fits for all possible values of $t_s^{\min}$ subject to the requirements that at least two t_s values enter the fit and that the number of degrees of freedom be strictly positive, thus defining a set Θ of $t_s^{\min}$ values on each gauge ensemble. At small values of t_s, contributions from excited states are expected to be significant, whereas at large t_s the signal-to-noise ratio becomes poor. This leaves us with a relatively small window of starting values $t_s^{\min}$ that can safely be used. Rather than choosing a single $t_s^{\min}$, we average the fit results $a_n(t_s^{\min})$ over all values $t_s^{\min} \in \Theta$, using as a weight factor a "smooth window" function $f(t_s^{\min})$,

$$a_n = \sum_{t_s^{\min}\in\Theta} f(t_s^{\min}) a_n(t_s^{\min}) \Big/ \left(\sum_{t_s^{\min}\in\Theta} f(t_s^{\min}) \right), \quad (12)$$

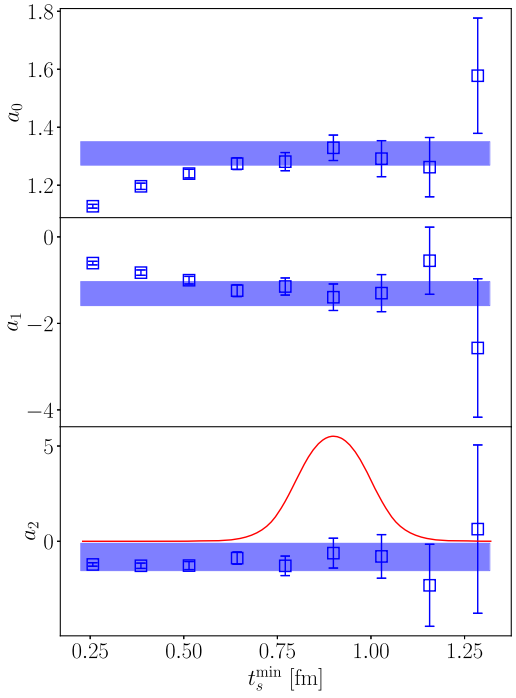

FIG. 1. Illustration of averaging over the minimum source-sink separation $t_s^{\min}$ in the summation method for the near-physical pion mass ensemble E250 of size 192×96^3 with a lattice spacing of 0.064 fm. We perform the z-expansion fits for each ensemble starting at different values of $t_s^{\min}$. The results for coefficients a_0, a_1 and a_2 are shown here as the blue squares. The bands represent the smooth-window averages over $t_s^{\min}$, and the solid red line shows the weight function Eq. (13) (arbitrarily normalized for visibility), which is applied to all three coefficients.

$$f(\tau) = \tanh\left(\frac{\tau - t_w^{\text{low}}}{\Delta t_w}\right) - \tanh\left(\frac{\tau - t_w^{\text{up}}}{\Delta t_w}\right), \quad (13)$$

with $t_w^{\text{low}} = 0.8$ fm, $t_w^{\text{up}} = 1.0$ fm and $\Delta t_w = 0.08$ fm. Note that neither the statistical errors nor the covariance matrix enter the average; the uncertainty on the latter is obtained via the standard jackknife method (see e.g., Ref. [24]). The average (12) represents very well what could be identified as a plateau in the fit results, as illustrated in Fig. 1. The three panels also illustrate the advantage of having to scrutinize only very few observables for excited-state effects, as opposed to having to do this for every Q^2 value. Having an extended set of t_s values at our disposal, the control over these effects is significantly improved as compared to our previous summation-method results for the vector form factors [18].

III. THE LATTICE CALCULATION

We use a set of 14 CLS (coordinated lattice simulations) $N_f = 2 + 1$ ensembles [25] that have been generated with nonperturbatively $\mathcal{O}(a)$-improved Wilson fermions [26,27] and the tree-level improved Lüscher-Weisz gauge action [28]. They cover the range of lattice spacings from 0.050 to 0.086 fm and pion masses from about 350 down to 130 MeV. Details of these ensembles, including the number of configurations, the number of measurements and the number of available source-sink separations t_s, are listed in Table I. All lattices used in this study have a fairly large volume, which is indicated by $M_\pi L \gtrsim 4$.

For most of these ensembles, the fields obey open boundary conditions in time [30] in order to prevent topological freezing [31]. The reweighting factors needed to correct for the treatment of the strange-quark determinant during the gauge field generation were computed using the method of Ref. [32]. Our setup to compute the nucleon two- and three-point functions is similar to that used in our study on the isovector charges of the nucleon [33].

As discussed in Sec. II, we perform simultaneous fits to all data points with $Q^2 \leq 0.7$ GeV^2 and source-sink separations $t_s \geq t_s^{\min}$ on each ensemble to obtain the coefficients $a_n(t_s^{\min})$ of the z expansion at the given pion mass, lattice spacing and volume. Subsequently, the averaged coefficients a_n are obtained via Eq. (12). Recall that in our analysis, we incorporate the z expansion, which parametrizes the Q^2 dependence of the form factor, directly into the summation method. This can also be done in two separate steps, first using the summation method to get the value of the form factor at a given Q^2, keeping track of the correlation between the data at different Q^2 values, and then parametrizing the Q^2 dependence of the form factor using a z expansion. The two methods should obviously give compatible results, which we find to be the case. This is illustrated in Fig. 2 on ensemble E250.

TABLE I. Overview of ensembles used in this study. The values $\beta = 3.40$, 3.46, 3.55 and 3.70 correspond to lattice spacings $a \approx 0.086$, 0.076, 0.064 and 0.050 fm, respectively [29]. Columns T/a and L/a give the temporal and spatial size of the lattice, and M_π and M_N are the pion and nucleon masses. N_{conf} is the number of configurations used for each ensemble, and in column N_{meas} we list the number of measurements done at the largest source-sink separation. To keep the signal-to-noise ratio as a function of t_s close to constant for decreasing t_s, the number of measurements is reduced by a factor of 2 in steps of $\Delta t_s \approx 0.2$ fm for the periodic ensembles E250, D450 and N451, while for all other ensembles this iterative reduction sets in only for $t_s < 1.0$ fm. N_{t_s} is the number of available source-sink separations in the range listed in column t_s. However, in this study the smooth window of Eq. (13) gives a strong weight to those values of t_s^{min} (the smallest value of t_s included in the summation method) in the range 0.8…1.0 fm.

ID	β	T/a	L/a	M_π [MeV]	$M_\pi L$	M_N [GeV]	N_{conf}	N_{meas}	t_s [fm]	N_{t_s}
H102	3.40	96	32	354	4.96	1.103	2005	32080	0.35…1.47	14
H105	3.40	96	32	280	3.93	1.045	1027	49296	0.35…1.47	14
C101	3.40	96	48	225	4.73	0.980	2000	64000	0.35…1.47	14
N101	3.40	128	48	281	5.91	1.030	1596	51072	0.35…1.47	14
S400	3.46	128	32	350	4.33	1.130	2873	45968	0.31…1.53	9
N451	3.46	128	48	286	5.31	1.045	1011	129408	0.31…1.53	9
D450	3.46	128	64	216	5.35	0.978	500	64000	0.31…1.53	17
N203	3.55	128	48	346	5.41	1.112	1543	24688	0.26…1.41	10
N200	3.55	128	48	281	4.39	1.063	1712	20544	0.26…1.41	10
D200	3.55	128	64	203	4.22	0.966	2000	64000	0.26…1.41	10
E250	3.55	192	96	129	4.04	0.928	400	102400	0.26…1.41	10
N302	3.70	128	48	348	4.22	1.146	2201	35216	0.20…1.40	13
J303	3.70	192	64	260	4.19	1.048	1073	17168	0.20…1.40	13
E300	3.70	192	96	174	4.21	0.962	570	18240	0.20…1.40	13

Our proposed method leads to larger correlation matrices, and in some cases small eigenvalues can cause difficulties in calculating the inverse of the matrix. If the resulting correlation matrix is larger than 70×70, then we slightly damp the off-diagonal correlations to avoid numerical instabilities [34], a procedure that has been used a number of times in lattice QCD calculations, see e.g., [35–38]. This regularization prescription reads

$$C_{ij}^{\text{reg}} = (1 - x)\delta_{ij}C_{ii} + xC_{ij} \tag{14}$$

(without any summation convention in place), and we have used $x = 0.985…0.995$. The one-step fits are then very stable and robust, and the damping of off-diagonal correlations essentially only affects the χ^2 of the fit. This is our preferred method, as it gives readily a parametrization of the shape of the form factor. The results of these fits are tabulated ensemble-by-ensemble in Table II in Appendix A.

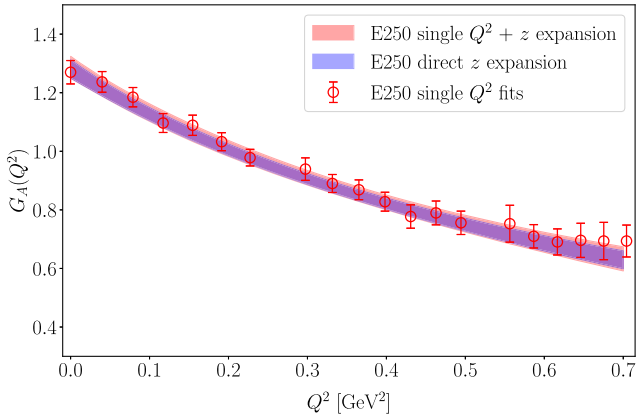

FIG. 2. Consistency check of the new method. We plot the results of fits to single Q^2 data (red data points) and compare them to the result of the immediate z expansion (the blue error band) on ensemble E250 using $t_s^{\text{min}} = 12$. The red error band is a z-expansion fit to the single Q^2 data points (including correlations), whereas the blue error band shows the fit where the z expansion is directly incorporated into the summation method [Eq. (9)]. Here $t_s^{\text{min}} = 12$. The agreement is good, and the immediate z expansion provides readily a model-independent parametrization of the shape of the form factor.

We then proceed to perform chiral and continuum extrapolations of the coefficients a_n to the physical point, including for each of them a term linear in a^2. As for their chiral behavior, we use the following three *Ansätze*:

(1) Linear in M_π^2 for all coefficients a_n.
(2) Again linear in M_π^2 for coefficients a_1 and a_2, and an extended *Ansatz* containing a chiral logarithm for the zeroth coefficient:

$$a_0 = g_a^{(0)} + g_a^{(1)}M_\pi^2 + g_a^{(3)}M_\pi^3 - g_a^{(2)}M_\pi^2 \ln\frac{M_\pi}{M_n}$$

with

$$g_a^{(1)} = 4d_{16} - \frac{(g_a^{(0)})^3}{16\pi^2 F_\pi^2},$$
$$g_a^{(2)} = \frac{g_a^{(0)}}{8\pi^2 F_\pi^2}(1 + 2(g_a^{(0)})^2),$$
$$g_a^{(3)} = \frac{g_a^{(0)}}{8\pi F_\pi^2 M_n}(1 + (g_a^{(0)})^2) - \frac{g_a^{(0)}}{6\pi F_\pi^2}\Delta_{c_3,c_4},$$

where $M_n = 938.92$ MeV is the nucleon mass and $F_\pi = 92.42$ MeV the pion decay constant [39]. Here $\Delta_{c_3,c_4} = c_3 - 2c_4$ is a combination of low-energy constants c_3 and c_4. The free fit parameters for the zeroth coefficient's chiral extrapolation are $g_a^{(0)}$, d_{16} and Δ_{c_3,c_4}.

(3) Same as *Ansatz* 2, but including M_π^3 terms for coefficients a_1 and a_2.

Note that, while the coefficients a_n do not have common fit parameters, they are correlated within an ensemble: these correlations are taken into account in the fits.

We perform multiple extrapolations using the different fit *Ansätze* described above with pion mass cuts $M_\pi < M_\pi^{\rm cut}$ with $M_\pi^{\rm cut}[\text{MeV}] \in \{300, 285, 265, 250\}$, as well as dropping data from the coarsest lattice spacing, to get a handle on systematic effects. Although we do not observe a strong dependence on the volume, we include a term [40]

$$\frac{M_\pi^2}{\sqrt{M_\pi L}} e^{-M_\pi L} \tag{15}$$

for the zeroth coefficient a_0 to check for possible finite-size effects (FSE) in some of the extrapolation fits. For a subset of fits, we impose Gaussian priors on the coefficients multiplying the a^2 terms, restricting the difference between the values at the coarsest lattice spacing and in the continuum limit to at most 20%. This is motivated by a tendency of these fits to attribute unnaturally large corrections to discretization effects, especially for a_1 and a_2 that are statistically less precise. We keep those fits that have a p value better than 5% and provide a satisfactory description of the data, especially at pion masses below 200 MeV. Some examples of these fits based on different *Ansätze* and pion mass cuts are shown in Appendix B.

While most of our fits have a good p value without including the FSE term of Eq. (15), which tends to slightly increase the uncertainties, we do include these fits in the analysis in order to account for the systematic effect due to finite-size corrections. Figure 3 illustrates this by comparing a selected fit, *Ansatz* 3 with a pion mass cut of 300 MeV, with and without the FSE term. We can also inspect finite-size effects directly by comparing our results of the z-expansion fits on two ensembles at a pion mass of 280 MeV, H105 and N101, which differ only by their spatial sizes, $L = 2.8$ and 4.1 fm, respectively. We show the results of the z-expansion fits on these two ensembles as a function of $t_s^{\rm min}$ in Fig. 4. We find that the coefficients a_n agree well, confirming that finite-size effects are small at the current level of precision.

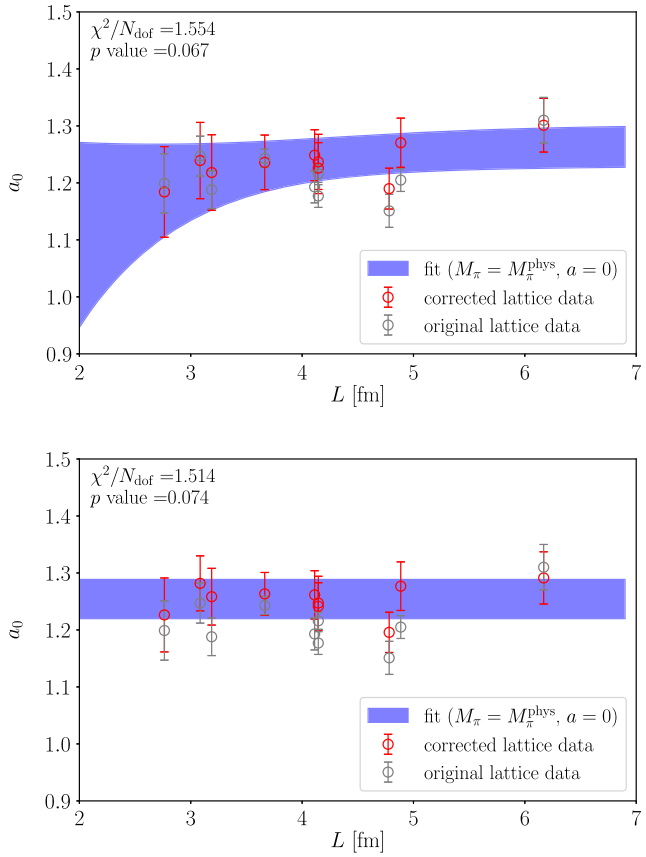

FIG. 3. Finite size effects: coefficient a_0 (the axial charge) from fit *Ansatz* 3 with a pion mass cut of 300 MeV, with and without the FSE term [Eq. (15)]. The two fits are equally good, and are both included in the AIC average.

Since different fit *Ansätze* and cuts can be equally well motivated, as in our previous study of the vector form factors of the nucleon [18] we perform a weighted average [41] over the resulting a_n, where the Akaike information criterion (AIC) [42] is used to weight different analyses and to estimate the systematic error associated with the variations of the global fit. Different versions of the AIC weights have been developed and used over the years. Here we choose [43]

$$w^{\rm AIC} = N e^{-\frac{1}{2}(\chi^2 + 2n_{\rm par} - n_{\rm data})}, \tag{16}$$

where the minimum χ^2, the number of fit parameters $n_{\rm par}$ and the number of data points $n_{\rm data}$ characterize the fit. N is a normalization factor that ensures that the sum of the weights is unity. The corresponding cumulative distribution functions of the coefficients a_n and of the mean square radius $\langle r_A^2 \rangle$ are well behaved and show no outliers. We determine the central value from the 50th percentile, and

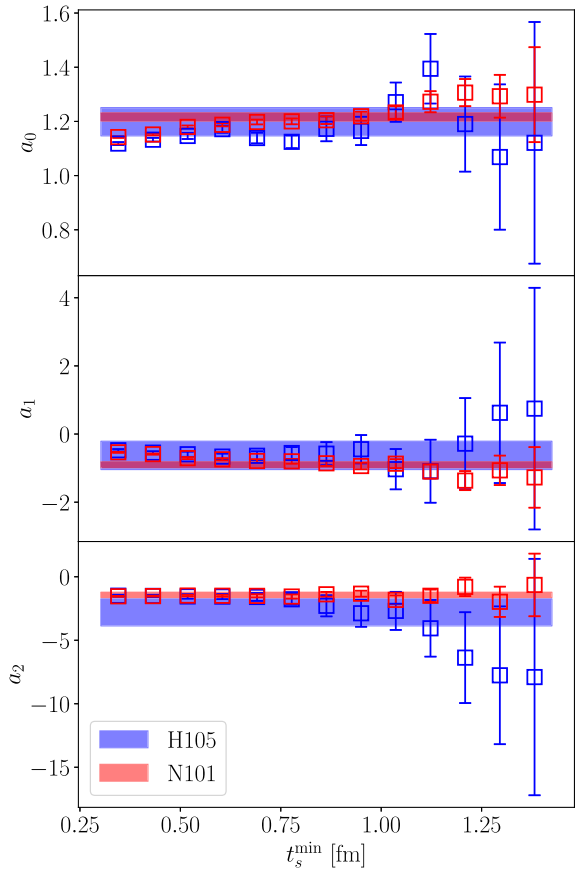

FIG. 4. Direct comparison of the data as a function of $t_s^{\min}$ and the "smooth window" average of Eq. (13) on two of the ensembles, H105 and N101. These ensembles have the same lattice spacing and quark masses, but differ by their volume. The data points show good agreement, which indicates that any finite size effects are small.

the full uncertainty as the interval from the 16th to the 84th percentile. The decomposition of the error into its statistical and systematic components is achieved following the prescription proposed in [43]. More details of the model averaging procedure are given in Appendix C.

IV. RESULTS

Our results for the coefficients of the z expansion of the nucleon axial form factor in the continuum and at the physical pion mass are

$$\begin{aligned} a_0 &= 1.225 \pm 0.039(\text{stat}) \pm 0.025(\text{syst}), \\ a_1 &= -1.274 \pm 0.237(\text{stat}) \pm 0.070(\text{syst}), \\ a_2 &= -0.379 \pm 0.592(\text{stat}) \pm 0.179(\text{syst}) \end{aligned} \tag{17}$$

with a correlation matrix

$$M_{\text{corr}} = \begin{pmatrix} 1.00000 & -0.67758 & 0.61681 \\ -0.67758 & 1.00000 & -0.91219 \\ 0.61681 & -0.91219 & 1.00000 \end{pmatrix}. \tag{18}$$

These results, meant to be inserted into Eqs. (10) and (11) with $t_{\text{cut}} = (3M_{\pi^0})^2$, lead to the following mean square radius:

$$\langle r_A^2 \rangle = (0.370 \pm 0.063(\text{stat}) \pm 0.016(\text{syst}))\ \text{fm}^2. \tag{19}$$

The axial charge $g_A = a_0$ is in good agreement with our previous determination [33] based on forward nucleon matrix elements only. Since the latter method tends to yield more precise results for a given dataset, we do not view the present determination of g_A as superseding that of Ref. [33], and merely perform the comparison as a consistency check.

To see how the corrections due to finite lattice spacing and finite volume affect the form factor, we can compare our final result to the form factor obtained on our physical pion mass ensemble, E250. This is illustrated in Fig. 5. At small Q^2 the corrections are clearly visible, whereas at large Q^2 the two results agree within a fraction of the error.

We compare our result to other lattice QCD determinations of the mean square radius in Fig. 6, finding good agreement within errors. The comparison features only lattice calculations with a full error budget, including a continuum extrapolation; see Refs. [12,14–16,44] for further lattice results. The NME21 result is from [11], and the RQCD20 result is from [13]. Both studies parametrize the Q^2 dependence of the form factor using a z expansion (RQCD also use a dipole *Ansatz* as an alternative parametrization, but that result is not shown in the figure). For comparison, we show the average of the values obtained from z-expansion fits to neutrino scattering and

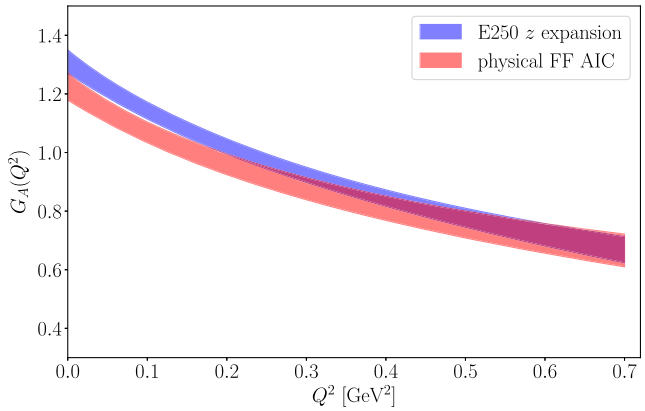

FIG. 5. Comparing our final result for the axial form factor, in the continuum and infinite volume limit at the physical pion mass, to our result on the physical mass ensemble E250. Any difference between the two error bands is due to finite lattice spacing and finite volume, and the comparison shows how large these corrections are as a function of Q^2.

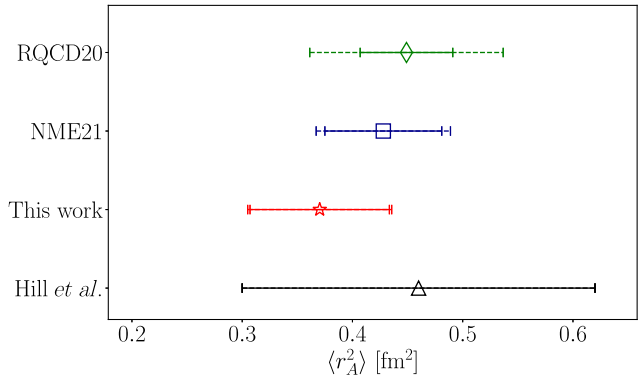

FIG. 6. Comparison of lattice determinations of the mean square radius $\langle r_A^2 \rangle$, from Refs. [11] (NME21) and [13] (RQCD20). The point labeled Hill *et al.* is an average of the values obtained from z-expansion fits to neutrino scattering and muon capture [17]. The smaller error bars with solid lines show the statistical errors, whereas the wider error bars with dashed lines show the total errors (including systematic uncertainties).

muon capture measurements [17]. Our result also agrees well with the earlier two-flavor calculation by the Mainz group [45], and with a more recent analysis [46] by the same group that has been obtained via the conventional two-step process of first determining the form factor at discrete Q^2 values and subsequently parametrizing it.

Perhaps even more interesting is the comparison of our result for the axial form factor to data from pion electroproduction experiments [4] and to a z-expansion fit to neutrino-Deuterium scattering data [47] in Fig. 7. While our result agrees well with other lattice QCD calculations,

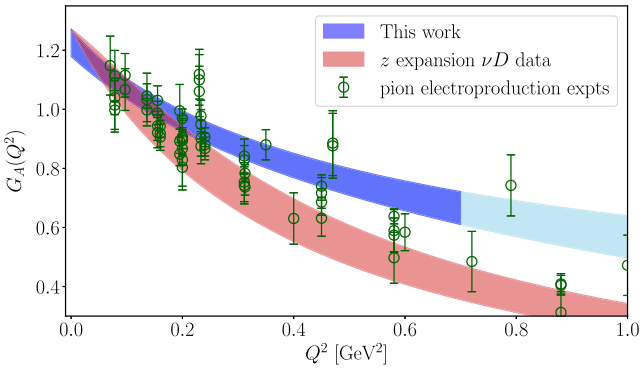

FIG. 7. Comparing our result for the axial form factor to data from pion electroproduction experiments [4] and to a z-expansion fit to neutrino-Deuterium scattering data [47]. There is a clear tension between the lattice QCD result and the z expansion extracted from deuterium bubble chamber data, especially at large Q^2. The darker blue error band highlights the Q^2 range of our lattice data. The data from electroproduction experiments has been multiplied by the current Particle Data Group value for the axial charge [49].

as can be seen by comparing this figure to Fig. 3 in the review [5], there is a tension with the axial form factor extracted from experimental deuterium bubble chamber data [47]. This tension is strongest at large Q^2, the deuterium extraction being lower than the lattice prediction. The authors of the Snowmass White Paper on Neutrino Scattering Measurements [48] remark that, when translated to the nucleon quasielastic cross section, this discrepancy suggests that a 30–40% increase would be needed for these two results to match. They also note that recent high-statistics data on nuclear targets cannot directly resolve such discrepancies due to nuclear modeling uncertainties, and that new elementary target neutrino data would provide a critical input to resolve such discrepancies.

V. CONCLUSIONS

In this paper, we have introduced a new method to extract the axial form factor of the nucleon. It combines two well-known methods into one analysis step: the summation method ensures that excited-state effects are sufficiently suppressed, and the z expansion readily provides the parametrization of the Q^2 dependence of the form factor. Our main results are the coefficients of the z expansion, given in Eq. (17). Systematic effects are included through AIC averaging, which also provides the breakup into statistical and systematic uncertainties and the correlations among the coefficients. Our results are statistics limited, implying that significant improvements are still straightforwardly possible, though computationally costly.

We observe good agreement with other lattice QCD determinations of the axial form factor, which means that the tension with the shape of the form factor extracted from deuterium bubble chamber data is further strengthened. Comparing our result for $a_0 \equiv G_A(0)$ to the Particle Data Group value for the axial charge, $g_A = 1.2754(13)$ [49], which one might view as a benchmark, we find agreement at the 1.1σ level. Also, using largely the same gauge ensembles as in this work, we have previously found a good overall agreement for the isovector vector form factors [18] with phenomenological determinations, which are far more precise than in the axial-vector case. Thus a nucleon axial form factor falling off less steeply than previously thought now appears more likely.

In the near future, we plan to perform a dedicated calculation of various forward nucleon matrix elements, including the axial charge, updating the results of Ref. [33].

ACKNOWLEDGMENTS

We thank Tim Harris, who was involved in the early stages of this project [50]. This work was supported in part by the European Research Council (ERC) under the European Unions Horizon 2020 research and innovation program through Grant Agreement No. 771971-SIMDAMA and by the Deutsche Forschungsgemeinschaft (DFG) through the

Collaborative Research Center SFB 1044 "The low-energy frontier of the Standard Model", under Grant No. HI 2048/1-2 (Project No. 399400745) and in the Cluster of Excellence Precision Physics, Fundamental Interactions and Structure of Matter (PRISMA+EXC 2118/1) funded by the DFG within the German Excellence strategy (Project ID 39083149). Calculations for this project were partly performed on the HPC clusters "Clover" and "HIMster2" at the Helmholtz Institute Mainz, and "Mogon 2" at Johannes Gutenberg-Universität Mainz. The authors gratefully acknowledge the Gauss Centre for Supercomputing e.V. [51] for funding this project by providing computing time on the GCS Supercomputer systems JUQUEEN and JUWELS at Jülich Supercomputing Centre (JSC) via Grants No. HMZ21, No. HMZ23 and No. HMZ36 [the latter through the John von Neumann Institute for Computing (NIC)], as well as on the GCS Supercomputer HAZELHEN at Höchstleistungsrechenzentrum Stuttgart [52] under project GCS-HQCD. Our programs use the QDP++ library [53] and deflated SAP + GCR solver from the openQCD package [54], while the contractions have been explicitly checked using [55]. We are grateful to our colleagues in the CLS initiative for sharing the gauge field configurations on which this work is based.

APPENDIX A: ENSEMBLE-BY-ENSEMBLE RESULTS

Table II collects the fit results for the z-expansion coefficients and their statistical correlations on each gauge ensemble.

APPENDIX B: EXTRAPOLATION TO THE PHYSICAL POINT

We include global fits with three different *Ansätze* for the chiral behavior of the form factor and several pion mass cuts in our final AIC average. We also take into account finite volume corrections by including a volume-dependent term [Eq. (15) in the main text] in some of our fits. We show examples of these global fits in Figs. 8, 9, and 3. Figure 9 highlights the difference between *Ansatz* 2 and *Ansatz* 3, whereas comparing Fig. 8 and the top panel of Fig. 9 shows *Ansatz* 3 with different pion mass cuts (300 and 265 MeV, respectively).

APPENDIX C: AKAIKE (AIC) MODEL AVERAGE

In this appendix, we give more details of the final step of the analysis, the model average based on the AIC. As discussed in Sec. III, we take systematic errors into account by performing an AIC-based average over a set of chiral, continuum and infinite-volume extrapolations. We choose the weight [43]

$$w_k^{\mathrm{AIC}} = N \mathrm{e}^{-\frac{1}{2}(\chi_k^2 + 2n_{\mathrm{par},k} - n_{\mathrm{data},k})},$$

where the χ_k^2, the number of fit parameters $n_{\mathrm{par},k}$ and the number of data points $n_{\mathrm{data},k}$ describe the kth global fit. The first two terms in the exponent correspond to the standard AIC, and the last term is introduced to take into account fits with different number of data points, i.e., fits with different cuts in pion mass or lattice spacing. The weights are normalized so that $\sum_i w_i = 1$.

TABLE II. Our results for the coefficients a_0, a_1, a_2 of the z expansion for each ensemble, as well as their correlations $\rho_{a_i,a_j} = (\langle a_i a_j\rangle - \langle a_i\rangle\langle a_j\rangle)/(\sqrt{\langle a_i^2\rangle - \langle a_i\rangle^2}\sqrt{\langle a_j^2\rangle - \langle a_j\rangle^2})$. These are smooth window averages [see Eq. (13)] of z-expansion fits to the sum $S(\vec{q}, t_s)$ in Eq. (9) using different t_s^{min}.

ID	a_0	a_1	a_2	ρ_{a_0,a_1}	ρ_{a_0,a_2}	ρ_{a_1,a_2}
C101	1.177(20)	−0.56(12)	−2.36(29)	−0.59707	0.30568	−0.85694
D200	1.193(28)	−1.07(17)	−1.01(42)	−0.58273	0.35465	−0.87957
D450	1.205(20)	−0.78(11)	−1.68(30)	−0.52813	0.13464	−0.76168
E250	1.310(40)	−1.31(28)	−0.82(72)	−0.61384	0.29885	−0.87065
E300	1.151(29)	−0.81(19)	−1.48(48)	−0.58834	0.31474	−0.88040
H102	1.157(16)	−0.55(11)	−2.01(33)	−0.39306	0.12100	−0.89438
H105	1.199(52)	−0.63(42)	−2.8(1.1)	−0.55469	0.33040	−0.93019
J303	1.188(33)	−0.89(20)	−1.05(52)	−0.59229	0.24273	−0.84407
N101	1.216(15)	−0.899(86)	−1.43(21)	−0.55315	0.22582	−0.81047
N200	1.247(35)	−0.71(21)	−1.76(54)	−0.53414	0.24793	−0.86773
N203	1.123(23)	−0.66(13)	−1.54(35)	−0.48820	0.18570	−0.83382
N302	1.164(34)	−0.64(26)	−2.36(70)	−0.48779	0.21775	−0.91619
N451	1.243(16)	−0.912(99)	−1.15(26)	−0.54656	0.27504	−0.84718
S400	1.178(23)	−0.47(18)	−1.99(51)	−0.44271	0.18507	−0.91340

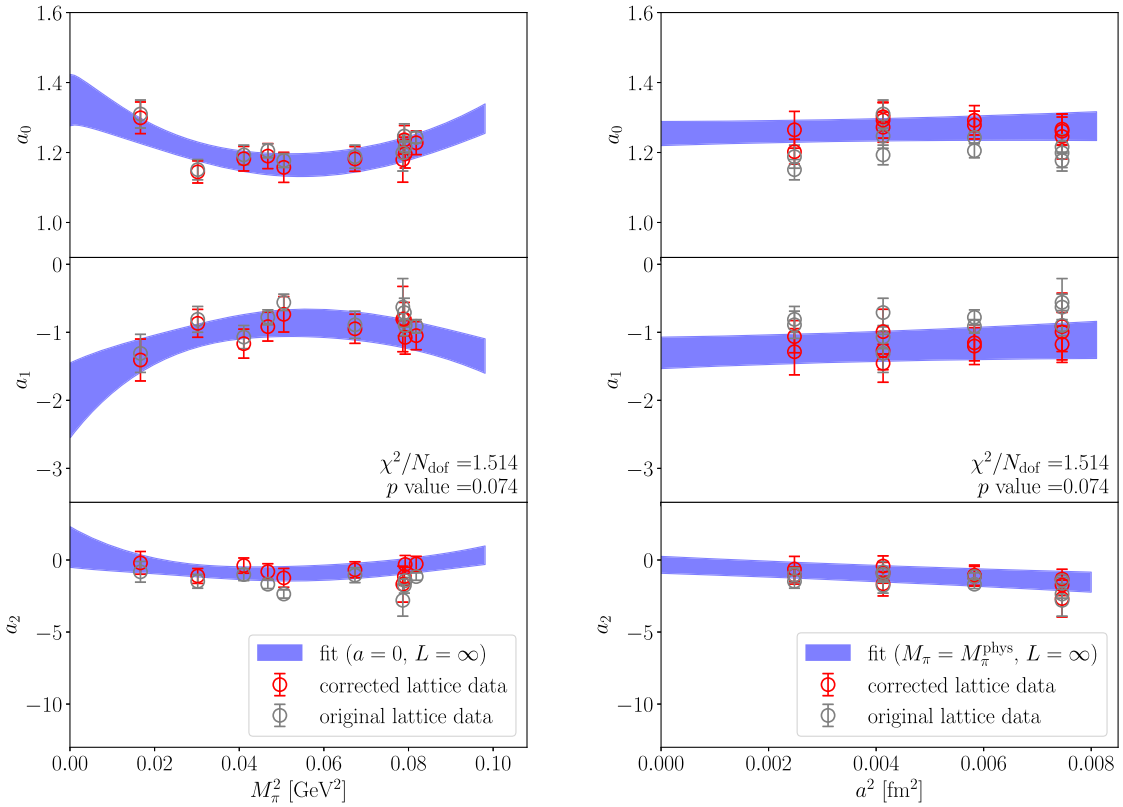

FIG. 8. Chiral and continuum extrapolations using fit *Ansatz* 3 (without the FSE term) and a pion mass cut of 300 MeV. The red circles show the corrected lattice data at infinite volume, and with zero lattice spacing or physical pion mass, respectively, in the left and right columns, whereas the gray data points are uncorrected.

The weights $w_i^{\rm AIC}$ are interpreted as probabilities, and the analyses follow a normal (Gaussian) distribution $N(a_i; m_k, \sigma_k)$ with a central value m_k and a standard deviation σ_k for the quantity a_i. m_k and σ_k are the jackknife average and the jackknife error in the kth analysis. A joint distribution function can then be defined as

$$\sum_k w_k^{\rm AIC} N(a_i; m_k, \sigma_k),$$

which includes both statistical and systematic uncertainties. The corresponding cumulative distribution function (CDF) reads

$$P(a_i) = \int_{-\infty}^{a_i} {\rm d}a_i' \sum_k w_k^{\rm AIC} N(a_i'; m_k, \sigma_k).$$

The median of the CDF gives the central value of a_i and its total error is given by the 16% and 84% percentiles of the CDF. Noticing that scaling σ_k by a factor of $\sqrt{\lambda}$ scales the statistical error by $\sqrt{\lambda}$, but does not scale the systematic error, we determine the breakup of the total uncertainty into statistical and systematic errors using $\lambda = 1$ and $\lambda = 2$.

In Fig. 10, we show the AIC averages and the corresponding cumulative distributions for all coefficients a_i as well as for the mean square radius $\langle r_A^2 \rangle$. These are all well behaved and contain no outliers. The data points are individual analyses, or fits, that give a good description of the data with a p value better than 5%. These are the analyses that enter the AIC procedure. The error band shows the AIC average with the total (statistical and systematic) uncertainty.

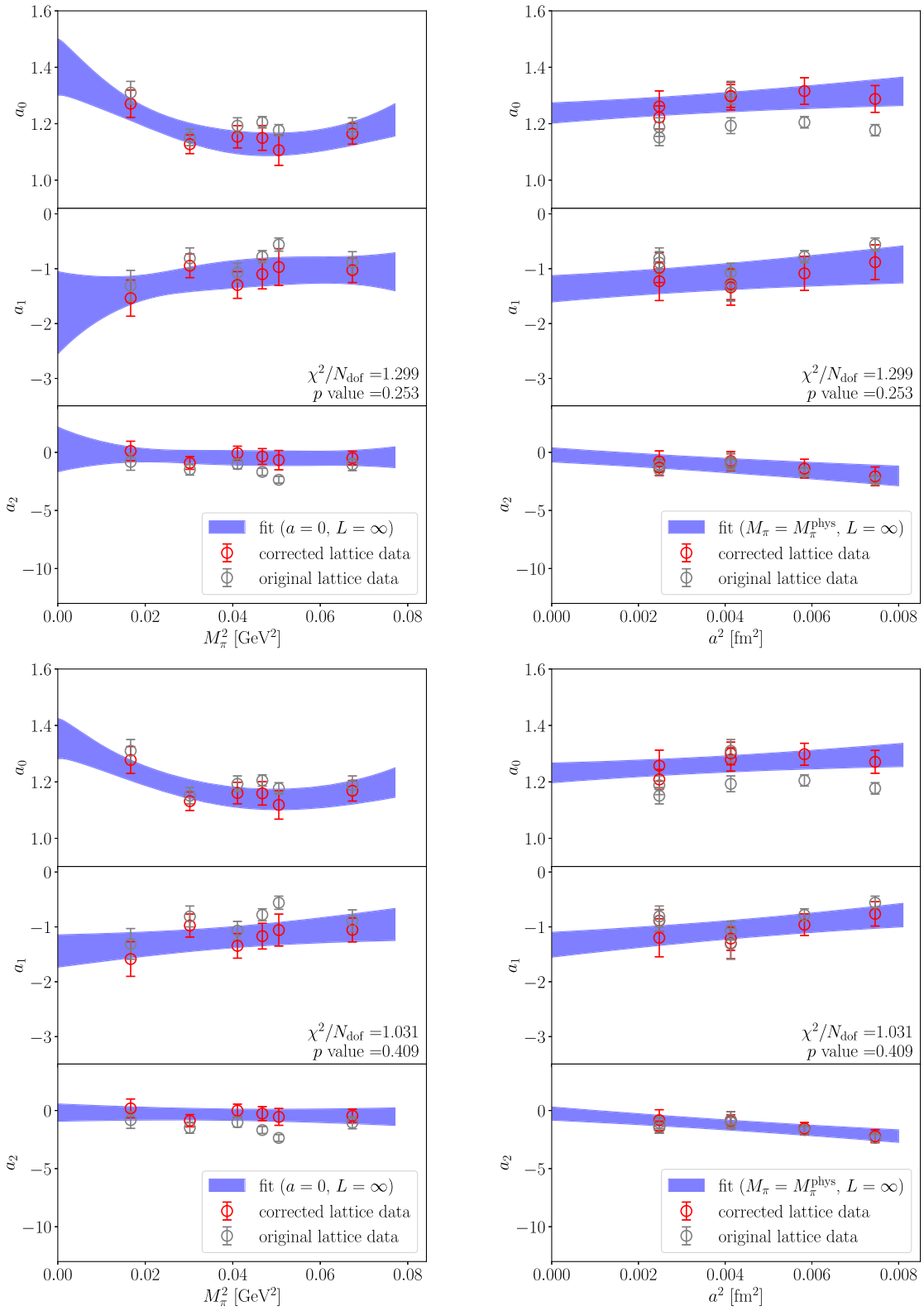

FIG. 9. Extrapolation in pion mass and lattice spacing using fit *Ansatz* 3 (top panel) and fit *Ansatz* 2 (lower panel) with a pion mass cut of 265 MeV. No FSE term was included in these fits. The red circles show the corrected lattice data at infinite volume, and with zero lattice spacing or physical pion mass, respectively, in the left and right columns, whereas the gray data points are uncorrected.

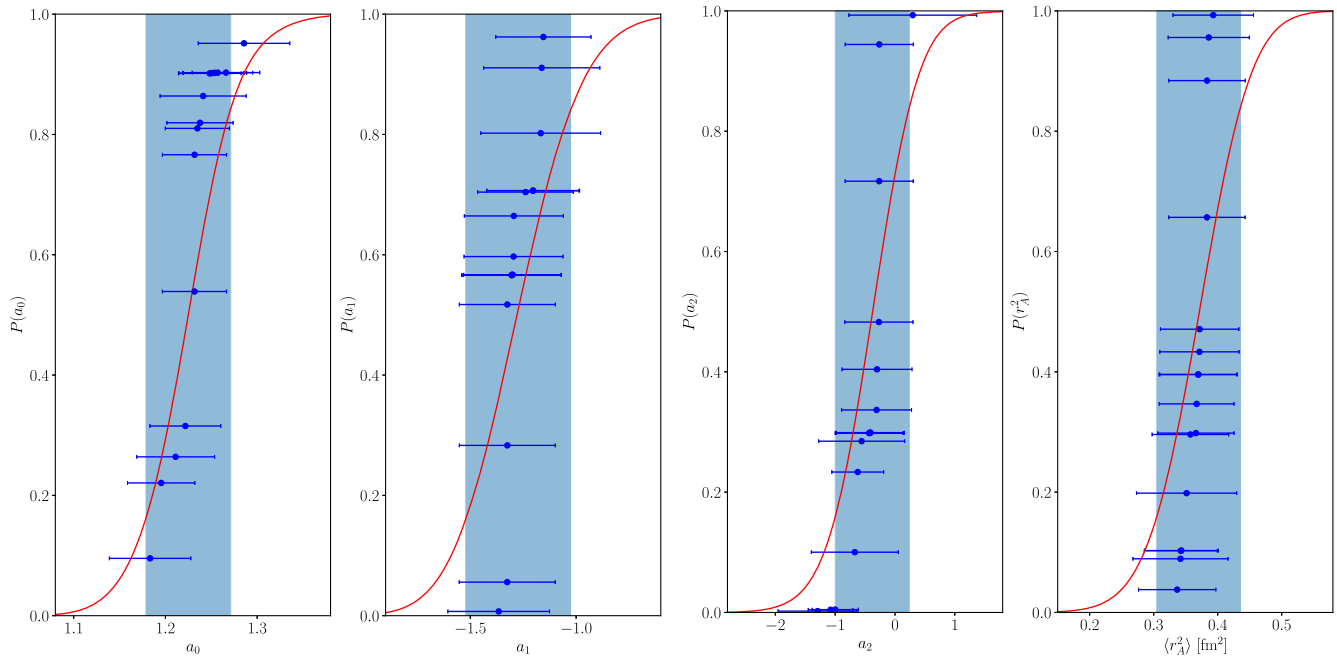

FIG. 10. AIC average and the corresponding cumulative distribution function for all coefficients a_0, a_1, a_2, and the mean square radius $\langle r_A^2 \rangle$ (in fm^2 units).

[1] R. Acciarri *et al.* (DUNE Collaboration), arXiv:1512.06148.
[2] K. Abe *et al.* (Hyper-Kamiokande Collaboration), arXiv:1805.04163.
[3] L. A. Ruso *et al.*, arXiv:2203.09030.
[4] V. Bernard, L. Elouadrhiri, and U.-G. Meissner, J. Phys. G **28**, R1 (2002).
[5] A. S. Meyer, A. Walker-Loud, and C. Wilkinson, Annu. Rev. Nucl. Part. Sci. **72**, 205 (2022).
[6] Y. Aoki *et al.*, arXiv:2111.09849.
[7] S. Capitani, B. Knippschild, M. Della Morte, and H. Wittig, Proc. Sci., LATTICE2010 (2010) 147.
[8] B. B. Brandt, S. Capitani, M. Della Morte, D. Djukanovic, J. Gegelia, G. von Hippel, A. Jüttner, B. Knippschild, H. B. Meyer, and H. Wittig, Eur. Phys. J. Special Topics **198**, 79 (2011).
[9] J. Green, Proc. Sci., LATTICE2018 (**2018**) 016.
[10] K. Ottnad, Eur. Phys. J. A **57**, 50 (2021).
[11] S. Park, R. Gupta, B. Yoon, S. Mondal, T. Bhattacharya, Y.-C. Jang, B. Joó, and F. Winter (Nucleon Matrix Elements (NME) Collaboration), Phys. Rev. D **105**, 054505 (2022).
[12] Y.-C. Jang, R. Gupta, B. Yoon, and T. Bhattacharya, Phys. Rev. Lett. **124**, 072002 (2020).
[13] G. S. Bali, L. Barca, S. Collins, M. Gruber, M. Löffler, A. Schäfer, W. Söldner, P. Wein, S. Weishäupl, and T. Wurm (RQCD Collaboration), J. High Energy Phys. 05 (2020) 126.
[14] C. Alexandrou *et al.*, Phys. Rev. D **103**, 034509 (2021).
[15] E. Shintani, K.-I. Ishikawa, Y. Kuramashi, S. Sasaki, and T. Yamazaki, Phys. Rev. D **99**, 014510 (2019); **102**, 019902(E) (2020).
[16] K.-I. Ishikawa, Y. Kuramashi, S. Sasaki, E. Shintani, and T. Yamazaki (PACS Collaboration), Phys. Rev. D **104**, 074514 (2021).
[17] R. J. Hill, P. Kammel, W. J. Marciano, and A. Sirlin, Rep. Prog. Phys. **81**, 096301 (2018).
[18] D. Djukanovic, T. Harris, G. von Hippel, P. M. Junnarkar, H. B. Meyer, D. Mohler, K. Ottnad, T. Schulz, J. Wilhelm, and H. Wittig, Phys. Rev. D **103**, 094522 (2021).
[19] S. Güsken, U. Löw, K. H. Mütter, R. Sommer, A. Patel, and K. Schilling, Phys. Lett. B **227**, 266 (1989).
[20] M. Albanese *et al.* (APE Collaboration), Phys. Lett. B **192**, 163 (1987).
[21] M. Dalla Brida, T. Korzec, S. Sint, and P. Vilaseca, Eur. Phys. J. C **79**, 23 (2019).
[22] P. Korcyl and G. S. Bali, Phys. Rev. D **95**, 014505 (2017).
[23] R. J. Hill and G. Paz, Phys. Rev. D **82**, 113005 (2010).
[24] Martin Lüscher, in *Les Houches Summer School: Session 93: Modern perspectives in Lattice QCD: Quantum Field Theory and High Performance Computing* (2010), pp. 331–399, arXiv:1002.4232.
[25] M. Bruno *et al.*, J. High Energy Phys. 02 (2015) 043.
[26] B. Sheikholeslami and R. Wohlert, Nucl. Phys. **B259**, 572 (1985).
[27] J. Bulava and S. Schaefer, Nucl. Phys. **B874**, 188 (2013).

[28] M. Lüscher and P. Weisz, Commun. Math. Phys. **97**, 59 (1985); **98**, 433(E) (1985).
[29] M. Bruno, T. Korzec, and S. Schaefer, Phys. Rev. D **95**, 074504 (2017).
[30] Martin Lüscher and Stefan Schaefer, J. High Energy Phys. 07 (2011) 036.
[31] S. Schaefer, R. Sommer, and F. Virotta (ALPHA Collaboration), Nucl. Phys. **B845**, 93 (2011).
[32] D. Mohler and S. Schaefer, Phys. Rev. D **102**, 074506 (2020).
[33] T. Harris, G. von Hippel, P. Junnarkar, H. B. Meyer, K. Ottnad, J. Wilhelm, H. Wittig, and L. Wrang, Phys. Rev. D **100**, 034513 (2019).
[34] A. Touloumis, Comput. Stat. Data Anal. **83**, 251 (2015).
[35] E. Rinaldi, S. Syritsyn, M. L. Wagman, M. I. Buchoff, C. Schroeder, and J. Wasem, Phys. Rev. D **99**, 074510 (2019).
[36] M. Cè, T. Harris, H. B. Meyer, A. Steinberg, and A. Toniato, Phys. Rev. D **102**, 091501 (2020).
[37] M. Cè, T. Harris, A. Krasniqi, H. B. Meyer, and C. Török, Phys. Rev. D **106**, 054501 (2022).
[38] M. Cè, A. Gérardin, G. von Hippel, H. B. Meyer, K. Miura, K. Ottnad, A. Risch, T. San José, J. Wilhelm, and H. Wittig, J. High Energy Phys. 08 (2022) 220.
[39] M. R. Schindler, T. Fuchs, J. Gegelia, and S. Scherer, Phys. Rev. C **75**, 025202 (2007).
[40] S. R. Beane and M. J. Savage, Phys. Rev. D **70**, 074029 (2004).
[41] W. I. Jay and E. T. Neil, Phys. Rev. D **103**, 114502 (2021).
[42] H. Akaike, IEEE Trans. Autom. Control **19**, 716 (1974).
[43] S. Borsanyi *et al.*, Nature (London) **593**, 51 (2021).
[44] N. Hasan, J. Green, S. Meinel, M. Engelhardt, S. Krieg, J. Negele, A. Pochinsky, and S. Syritsyn, Phys. Rev. D **97**, 034504 (2018).
[45] S. Capitani, M. Della Morte, D. Djukanovic, G. M. von Hippel, J. Hua, B. Jäger, P. M. Junnarkar, H. B. Meyer, T. D. Rae, and H. Wittig, Int. J. Mod. Phys. A **34**, 1950009 (2019).
[46] T. Schulz, D. Djukanovic, G. von Hippel, J. Koponen, H. B. Meyer, K. Ottnad, and H. Wittig, Proc. Sci., LATTICE2021 (**2022**) 577.
[47] A. S. Meyer, M. Betancourt, R. Gran, and R. J. Hill, Phys. Rev. D **93**, 113015 (2016).
[48] L. Alvarez-Ruso *et al.*, arXiv:2203.11298.
[49] R. Workman *et al.* (Particle Data Group), Prog. Theor. Exp. Phys. **2022**, 083C01 (2022).
[50] B. B. Brandt, A. Francis, T. Harris, H. B. Meyer, and A. Steinberg, EPJ Web Conf. **175**, 07044 (2018).
[51] www.gauss-centre.eu.
[52] www.hlrs.de.
[53] Robert G. Edwards and Bálint Joó (SciDAC, LHPC, UKQCD Collaborations), Nucl. Phys. B, Proc. Suppl. **140**, 832 (2005).
[54] Martin Lüscher and Stefan Schaefer, Comput. Phys. Commun. **184**, 519 (2013).
[55] D. Djukanovic, Comput. Phys. Commun. **247**, 106950 (2020).